One-Pot Synthesis of Tin-Embedded Carbon/Silica Nanocomposites for Anode Materials in Lithium-Ion Batteries

Jongkook Hwang,[†] Seung Hee Woo,[‡] Jongmin Shim,[†] Changshin Jo,[†] Kyu Tae Lee,[‡,*] and Jinwoo Lee[†,*]

[†]Department of Chemical Engineering, Pohang University of Science and Technology (POSTECH), Pohang, Kyungbuk 790-784, Korea and [‡]Interdisciplinary School of Green Energy, Ulsan National Institute of Science and Technology (UNIST), Ulsan 689-798, Korea

ABSTRACT We report a facile "one-pot" method for the synthesis of Sn-embedded carbon–silica (CS) mesostructured (nanostructured) composites through the selective interaction of resol (carbon precursor), tetraethylorthosilicate (TEOS), and tributylphenyltin (Sn precursor) with an amphiphilic diblock copolymer, poly(ethylene oxide-*b*-styrene), PEO-*b*-PS. A unique morphology transition from Sn nanowires to spherical Sn nanoparticles embedded in CS framework has been obtained. Metallic Sn species are homogeneously embedded in a rigid CS framework and are effectively confined within the nanostructures. The resulting composites are used as anode materials for lithium-ion batteries and exhibit high specific capacities (600 mA h g^{-1} at a current density of 45 mA g^{-1}, and 440 mA h g^{-1} at a current density of 300 mA g^{-1}) and an excellent cyclability of over 100 cycles with high Coulombic efficiency. Most of all, the novel method developed in this work for synthesizing functional hybrid materials can be extended to the preparation of various functional nanocomposites owing to its versatility and facileness.

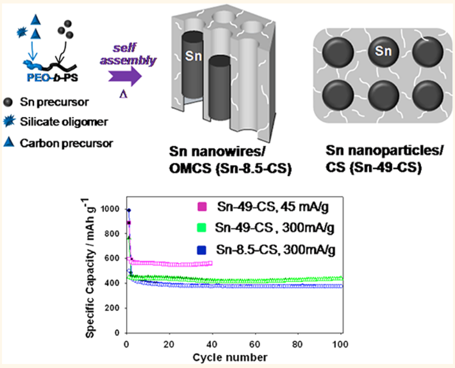

KEYWORDS: block copolymer · self-assembly · nanocomposites · anodes · lithium-ion batteries

Lithium-ion batteries (LIBs) are one of the promising energy storage devices for mobile devices and electric vehicles owing to their high power and high energy densities.[1,2] Pure metallic Sn has attracted considerable attention as an anode material for LIBs owing to its high theoretical specific capacity (992 mA h g^{-1}), which is 3 times that of commercialized graphite (372 mA h g^{-1}),[3,4] and high reversible capacity compared to Sn-oxides.[5] Nevertheless, the practical application of metallic Sn in LIBs is still quite challenging because Sn usually suffers from a significant change in volume during Li$^+$ insertion and extraction, resulting in the pulverization of electrodes and a rapid loss in capacity.[4,5] The aggregation of Sn nanoparticles upon cycling also reduces the cyclability of the electrodes.[6]

Recently, a substantial amount of effort has been made to tackle these problems, including the formation of nanostructured composites of Sn (or Sn-based materials) and carbon. Considerable improvements in the electrochemical property of LIBs have been achieved using designed nanocomposite materials.[7−19] In particular, ordered mesoporous carbon (OMC)[20,21] has been successfully employed in the preparation of electrochemically active composites, providing not only uniformly distributed pores that can act as a buffer for volume change but also high volume and high surface area for achieving a large uptake of active species. To prepare OMC-based composite materials, a host–guest approach[22] that employs OMCs as host and active species as guest has been popularly adopted. However, the implementation of this approach has been hampered by tedious and complicated steps that are necessary for preparing only the OMC itself, as well as the subsequent backfilling of active species into premade OMC through multiple impregnations.[23−26] Besides, some of the previously reported methods have suffered from poor impregnation[9] and a low loading of Sn species,[10,11,13] as well as residual Sn oxides,[9,12,16] which limit the overall capacity.

* Address correspondence to
ktlee@unist.ac.kr,
jinwoo03@postech.ac.kr.

Received for review August 7, 2012
and accepted January 14, 2013.

Published online January 14, 2013
10.1021/nn303570s

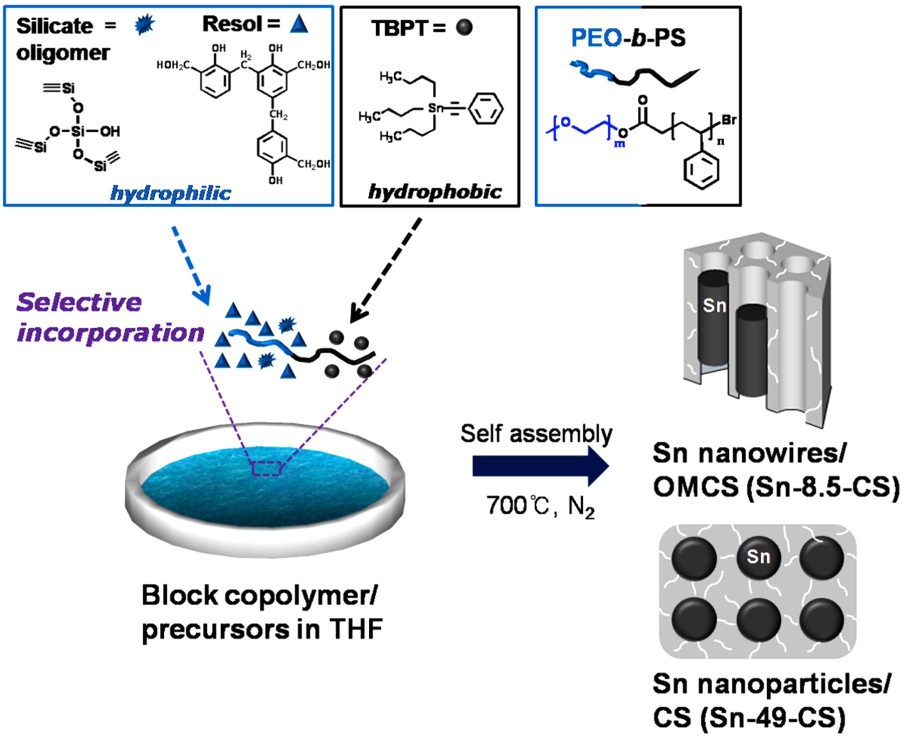

Scheme 1. Schematic representation of the synthesis of Sn/carbon–silica composites (Sn–CS); metallic Sn species are effectively confined in the CS matrix with the morphologies of nanowires or nanoparticles depending on the initial TBPT loading.

In this context, the development of a simple synthetic pathway to Sn-mesostructured (nanostructured) carbon composites with high reversible capacity and improved cyclability is still necessary.

Herein, we report a facile "one-pot" method[27,28] for the synthesis of Sn–carbon–silica (Sn–CS) mesostructured (nanostructured) composites as anodes for LIBs. Laboratory-synthesized poly(ethylene oxide-*b*-styrene) (PEO-*b*-PS) simultaneously directs the hydrophobic Sn precursor as well as hydrophilic carbon and silicate precursors into mesostructured (nanostructured) composites. Pure metallic Sn species are homogeneously embedded in the carbon–silica framework with the unique morphologies of nanowires or nanoparticles after heat treatment at 700 °C. The resulting Sn–CS composites are successfully employed as anode materials for LIBs, and they exhibit high capacity (600 mA h g^{-1} at a current density of 45 mA g^{-1}, and 440 mA h g^{-1} at a current density of 300 mA g^{-1}) and excellent cyclability (over 100 cycles). Compared with the backfilling methods employing OMCs as host materials,[23–26] the method in this paper eliminates tedious fabrication steps such as the preparation of OMC, impregnation of metal precursors inside the mesopores, and subsequent heat treatment. In addition, the method uses a straightforward pathway which can be extended to the preparation of various functional nanocomposites.

RESULTS AND DISCUSSION

Synthesis of Sn–CS Composites. Scheme 1 shows a general synthetic route for composite materials. The materials are obtained using the selective interaction of resol (nongraphitic carbon precursor), tetraethylorthosilicate (TEOS, silica precursor), and tributylphenyltin (TBPT, Sn precursor) with an amphiphilic diblock copolymer, poly(ethylene oxide-*b*-styrene), PEO_{118}-*b*-PS_{307}. A small amount of 0.2 M HCl is also added to hydrolyze TEOS to silicate oligomers. Laboratory-synthesized PEO-*b*-PS was chosen as a structure-directing agent because of a sufficient difference in the hydrophilicity and hydrophobicity of each block, which enables the selective inclusion of functional molecules to either type of block; it should also be noted that PEO-*b*-PS can be easily prepared without experience in polymer synthesis through a facile ATRP (atom transfer radical polymerization).[29,30]

Hydrophilic resol and silicate oligomers possess multiple hydroxyl groups, and thus, both precursors can strongly interact with the PEO block through hydrogen bonds. Meanwhile, the hydrophobic Sn precursor (TBPT) selectively interacts with the PS block owing to a hydrophobic–hydrophobic interaction. The mixture of precursors and PEO_{118}-*b*-PS_{307} is self-organized into ordered nanostructures under the process of evaporation-induced self-assembly (EISA) at 30 °C. The thermopolymerization step at 100 °C further induced cross-linkage and polymerization of the resol resins and froze the overall frameworks. The as-synthesized materials undergo heat treatment at 700 °C for 2 h under a N_2 atmosphere, during which the TBPTs are thermally decomposed into Sn metal and the PS block is converted to amorphous carbon in a confined space

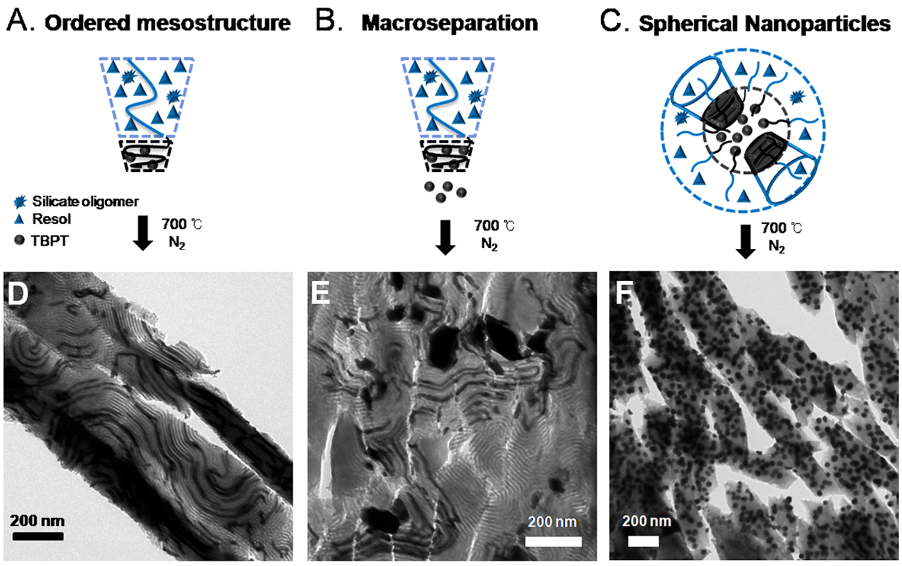

Figure 1. Suggested micelle structure of (A) ordered mesostructure with Sn nanowires (Sn-8.5-CS), (B) macroseparation between Sn nanowire/OMCS phase and the large-sized Sn-rich phase (Sn-14-CS), (C) spherical nanoparticles embedded in CS framework (Sn-49-CS), and corresponding microtomed transmission electron microscopy (TEM) image of (D) Sn-8.5-CS, (E) Sn-14-CS, and (F) Sn-49-CS.

owing to the presence of sp^2-hybridized carbon[30,31] in benzene rings. Simultaneously, the resol and silicate are transformed into rigid carbon–silica (CS) composites, while the PEO block is decomposed.

In this work, we fix the relative mass ratio of the final C/S as 8/2. A small amount of rigid silica acts as a reinforcing steel bar, improving the mechanical and thermal properties, and thus inhibiting framework shrinkage during carbonization at high temperature.[32] The resulting materials are denoted as Sn-*x*-CS, where *x* ranging from 0 to 49 represents the weight percentage of metallic Sn based on the final composite after heat treatment at 700 °C. The actual Sn content of each composite was determined by inductively coupled plasma spectroscopy (ICP). The weight fraction of each component is summarized in Table S1 of Supporting Information.

We start from ordered mesoporous carbon–silica (OMCS) without Sn content; Sn-0-CS. Tailored control of the volume fraction of each component[32–34] provides an ordered 2D hexagonal mesostructure of Sn-0-CS (Figure S1A). The relative mass ratio of carbon/silica is 8/2, which was determined by thermogravimetric analysis (TGA) in air (Figure S1B). To accommodate a high content of Sn metal, we intentionally increase the amount of TBPT, while the amounts of the other materials remain constant. Depending on the TBPT loading, morphologies from Sn nanowires (Sn-8.5-CS) to spherical Sn nanoparticles (Sn-26-CS and Sn-49-CS) have been obtained. Sn-8.5-CS forms an ordered CS framework with Sn nanowires grown along the cylindrical channel. This indicates that the PS block exclusively solvates the hydrophobic TBPT (Figure 1A) and that the TBPT is transformed into metallic Sn nanowires owing to the aggregation of Sn metals under heat treatment at 700 °C (Figure 1D). Due to the low melting point of Sn metal (232 °C), the molten Sn is mobile at the reaction temperature (700 °C) but still confined within the nanochannels of OMCS possibly by capillary force. It results in nanowire morphologies shaped by the rigid CS framework acting as a hard template. Many empty channels are produced because of the volume shrinkage during thermal decomposition of TBPT,[16] the aggregation of neighboring Sn droplets, and the volume shrinkage of molten Sn upon the cooling process, in consecutive order.[17–19]

A further increase in TBPT to obtain Sn-14-CS leads to a macrophase separation between the Sn nanowire/OMCS phase and the large-sized Sn-rich phase. Oily TBPT is solvated in the PS block until saturation, and remaining TBPT is expelled from the mesostructure during self-assembly (Figure 1B), resulting in the self-aggregation into large-sized Sn particles surrounded by mesostructure after heat treatment at 700 °C (Figure 1E). In other words, an excessive amount of TBPT cannot be fully accommodated in the PS microdomain, and therefore, a phase separation of the ordered mesostructure and large Sn particles simultaneously occurs. This can be further understood by introducing an A–B/C polymer blend system. A PS-*b*-(PEO/resol silicate)/TBPT hybrid system can be expected to behave similarly as an A–B diblock copolymer/C homopolymer system. The PS is an A block, and (PEO/resol silicate) can be considered a B block because resol and silicate are strongly incorporated into the PEO block through hydrogen bonds.[34] The TBPT can be regarded as a C homopolymer, which is chemically different but yet compatible with the A block, PS. In a real A–B/C polymer blend system, similar phenomena to those described above have been previously

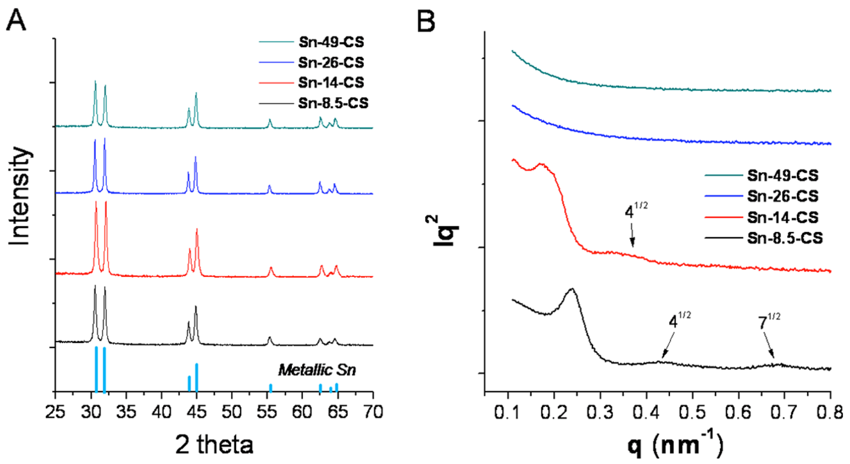

Figure 2. (A) X-ray diffraction (XRD) pattern of each Sn−CS composite material. The light-blue-colored bars indicate metallic β-Sn phase, JCPDS #86-2265 and (B) small-angle X-ray scattering (SAXS) pattern of each Sn−CS composite material.

demonstrated through both theoretical and experimental approaches.[35,36]

However, when we further increase the amount of TBPT, a unique nanostructure is observed, in which uniform-sized Sn nanoparticles are embedded in the CS matrix (Sn-26-CS, Figure S2; and Sn-49-CS, Figure 1F). In general, a polymer blend system is self-assembled to nanostructures in which the minority components are embedded into the matrix of the majority components.[35−38] In contrast, our hybrid system generates Sn nanoparticles in the CS matrix even at a high TBPT loading (as summarized in Table S2, the weight fraction of the hydrophobic contents, PS and TBPT, starts to exceed that of hydrophilic contents from Sn-26-CS). In a previous work on the synthesis of large-sized mesoporous silica, Stucky *et al.* reported a similar phase transition.[39] The authors added hydrophobic trimethylbenzene (TMB) to an aqueous P123 solution to expand the pore size of SBA-15. When a substantial amount of TMB was added, a sudden phase transition from a hexagonal (SBA-15, ∼11 nm) to a mesocellular form (MCF, ∼22 nm) consisting of uniform-sized spherical cells occurred. The authors claim that this transition was driven by the requirement to cover the oily TMB with a minimum amount of polymer. Through the transition of 11 nm diameter cylinders to 22 nm diameter spheres, the overall surface-to-volume ratio decreased by ∼30%.[40] Likewise, the formation of uniform-sized Sn nanoparticles in a large amount of excess TBPT might be driven by the need to decrease the surface-to-volume ratio with a fixed amount of PEO-*b*-PS. After the macroseparated structure intermediate (Sn-14-CS), the phase transition starts to stabilize excess TBPT expelled from the PS segments. As described in Figure 1C, TBPT is stabilized between the PS−PS segments owing to its innate incompatibility with PEO/resol silicate species. The transition from Sn nanowires, 17.9 nm in diameter, to Sn nanoparticles, 35.9 nm in diameter, stabilizes more TBPT with a fixed amount of PEO-*b*-PS and reduces the overall surface-to-volume ratio (Figure S3). Instead of generating pores after heat treatment, the TBPT is transformed into spherical Sn nanoparticles (Figure 1F). It should be emphasized that uniform-sized Sn nanoparticles are homogeneously embedded in the CS framework without any aggregation, which is probably due to a confinement effect in spherical pores and the *in situ* formed carbon from the PS segments, inhibiting particle growth in a confined space. As a result, mobile Sn species are well confined in the nanostructure rather than aggregated together to form large particles even at 700 °C. Further detailed aspects of the phase transition and formation mechanism of these novel materials are still being investigated.

The XRD results of each Sn-*x*-CS correspond to a pure metallic Sn phase without the presence of any crystalline Sn-oxides (Figure 2A). The amorphous Sn-oxides are still confirmed by the Sn 3d$_{5/2}$ peak in the X-ray photoelectron spectroscopy (XPS) spectrum, which corresponds to the binding energy of 486.6 eV (Figure S4). It indicates the surface oxidation of the metallic Sn nanoparticles which commonly occurs under ambient conditions.[41,42] The average crystallite size of Sn-8.5-CS, Sn-14-CS, Sn-26-CS, and Sn-49-CS is determined based on the Debye−Scherer equation and is estimated to be 17.9, 35.9, 35.4, and 35.9 nm, respectively. In the case of Sn-8.5-CS, the particle size is 17.9 nm, which is consistent with the pore size of OMCS, 17.3 nm, indicating that the Sn nanowires are generated by the aggregation of small Sn nanoparticles and effectively confined within the nanochannels of OMCS. Even particles larger than 100 nm are shown in the TEM image of Sn-14-CS, where the average particle size is 35.9 nm, suggesting that the portion of large segregated particles is relatively small compared to that of Sn nanowires. The average particle size of the spherical nanoparticles is around 35 nm in both Sn-26-CS and Sn-49-CS, which is also in good agreement with the

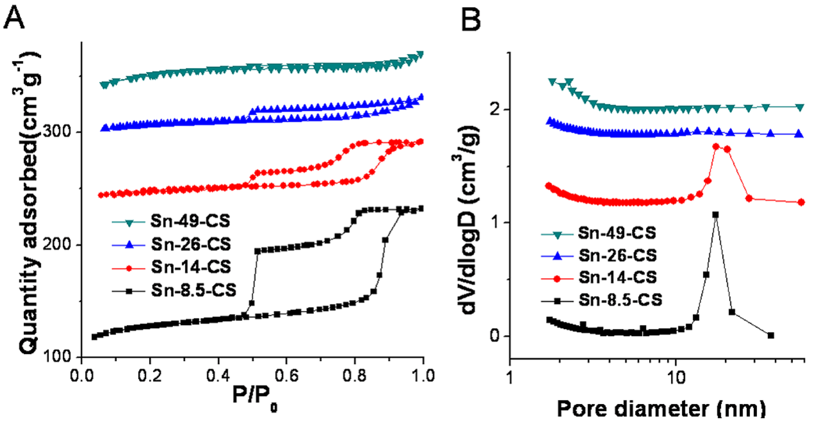

Figure 3. (A) N_2 sorption isotherm and (B) pore size distribution of each Sn–CS composite material.

TEM images. To further clarify this point, particle size distribution of Sn-49-CS was analyzed by counting 300 nanoparticles from the TEM image (Figure S5).

Figure 2B shows SAXS patterns of Sn-*x*-CS after carbonization. Sn-8.5-CS shows typical patterns of an ordered cylindrical mesostructure with relative scattering vector positions $3^{1/2}$, $4^{1/2}$, and $7^{1/2}$ of the first-order maximum. Sn-14-CS exhibits broad and unstructured peaks compared to Sn-8.5-CS, as it has a relatively short-range-ordered structure with large-sized Sn particles. No specific patterns are observed from Sn-26-CS owing to the loss of its ordered mesostructure. The SAXS results are consistent with the TEM images, suggesting the occurrence of a phase transition from an ordered cylindrical structure to a disordered structure.

A N_2 physisorption experiment further reveals the structural characteristics of the resulting composite materials. The nitrogen sorption isotherms of Sn-0-CS (Figure S1C), Sn-8.5-CS, and Sn-14-CS show typical type IV isotherms with a sharp adsorption at 0.95 P/P_0, indicating that uniform mesopores are well developed and dominant (Figure 3A). On the other hand, typical isotherms of the microporous materials are obtained for Sn-26-CS and Sn-49-CS. The pore size distribution is determined from the adsorption branch of the isotherm based on the Barrett–Joyner–Halenda (BJH) model. Narrow pore size distributions with a similar mean value of 17.3 nm are obtained for mesoporous Sn-0-CS, Sn-8.5-CS, and Sn-14-CS. The physiochemical properties of the Sn–CS composites are summarized in Table 1. As confirmed in TEM and SAXS, N_2 sorption analysis also suggests a phase transition from ordered mesostructure to disordered microporous structure. The mesopore volume (V_{meso}) starts to decrease dramatically from Sn-14-CS, and only a little fraction of V_{meso} remains in Sn-49-CS. The interpenetrating micropores generated under the calcinations of PEO segments[32] provide a micropore volume and a large surface area for all composite materials. The surface areas of the Sn–CS composite decreases as the weight percentage of Sn metal increases. Even their losses of the ordered mesostructure, Sn-26-CS, and Sn-49-CS have relatively large surface area and micropore volume. This may be attributed to the additional void space which is produced by volume shrinkage of metallic Sn (from the liquid to the solid state) during the cooling process.[19]

TABLE 1. Physiochemical Properties of the Sn–CS Composites

sample	D^a (nm)	$V_{meso}{}^b$ (cm^3/g)	$V_{micro}{}^c$ (cm^3/g)	$S_{BET}{}^d$ (m^2/g)
Sn-0-CS	17.3	0.23	0.15	436
Sn-8.5-CS	17.3	0.20	0.16	427
Sn-14-CS	17.4	0.10	0.15	408
Sn-26-CS		0.05	0.16	376
Sn-49-CS		0.01	0.17	326

[a] Calculated pore diameter from the adsorption branch on the basis of the BJH model. [b] Mesopore volume, $V_{total} - V_{micro}$. [c] T-plot micropore volume. [d] Specific suface area.

Resol used in this work is known to be a nongraphitizable amorphous carbon source which is difficult to graphitize at any heat treatment temperature.[43] In nongraphitic carbons, a number of single graphene sheets are arranged like a "house of cards" rather than stacked in a parallel way.[44] Figure 4 shows Raman spectra of Sn-0-CS, Sn-8.5-CS, and Sn-49-CS, indicating the presence of amorphous carbon in the composites. All spectra have two broad peaks at 1342 and 1600 cm^{-1} that can be assigned to the D and G bands, respectively. In the case of amorphous carbon, the G peak arises from stretching of any pair of sp^2 sites whether in rings or chains, thus the existence of a G peak does not imply graphite. The D peak arises from the breathing mode of sp^2 sites in rings, not chains. In addition, all Sn–CS composites have a low I_D/I_G intensity ratio near 0.80 and a broad G line width of 90 cm^{-1}, indicating a graphitic cluster size of amorphous carbon smaller than 10 Å.[45,46]

To verify whether lab-made PEO-*b*-PS is indispensable for synthesizing Sn particles confined inside a carbon–silica framework, we employed the commercial

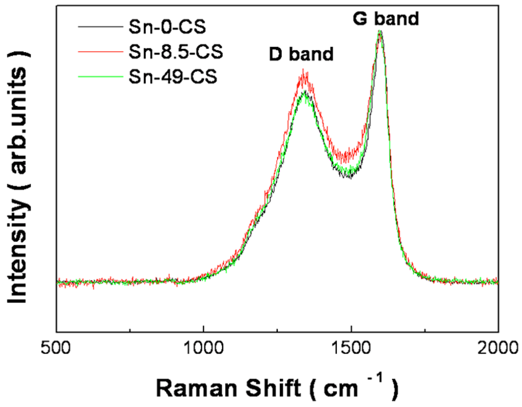

Figure 4. Raman spectra of representative Sn-0-CS (OMCS), Sn-8.5-CS, and Sn-49-CS.

F127 ($(EO)_{106}(PO)_{70}(EO)_{106}$) as a structure-directing agent with similar synthetic conditions found in Sn-8.5-CS. As shown in Figure S6A in Supporting Information, ordered mesostructure is lost even at a low loading of TBPT, Sn particles are poorly dispersed on the overall CS framework, and some of the particles are aggregated. The average particle size is determined to be 29 nm (from XRD, Figure S6B), which is much larger than the channel size of the mesoporous CS prepared by F127 (∼5 nm, Figure S6C). It indicates that most of Sn particles are nonselectively dispersed rather than confined in the mesostructure. Because of an insufficient difference in the hydrophilicity and hydrophobicity of the EO and PO blocks, F127 fails to induce a selective incorporation of guest molecules into the desired block.

Notably, the strategy for preparing a Sn–CS composite can be easily applied to the development of various kinds of functional materials. For instance, an intermetallic SnSb–CS composite was successfully synthesized by simply changing the hydrophobic precursor of the initial solution. An equimolar amount of hydrophobic Sn and Sb precursor provided an intermetallic SnSb–CS composite with a similar phase transition and material characteristics (Figure S7).

Electrochemical Performance. Figure 5 shows the electrochemical performance of Sn-8.5-CS and Sn-49-CS electrodes. Both Sn-8.5-CS and Sn-49-CS electrodes show an excellent cycle performance, as can be seen in Figure 5A. It is notable that no capacity fading was observed even after 100 cycles. This is attributed to the fact that Sn nanowires or nanoparticles are homogeneously embedded within the CS composite matrix. The CS framework acts as a protective barrier, minimizing direct contact between nanosized Sn particles, thus it suppresses the electrode degradation effectively by inhibiting the agglomeration of Sn nanowires and nanoparticles upon cycling. The Sn-49-CS electrode delivers a reversible capacity of 600 and 440 mA h g^{-1} at a current density of 45 and 300 mA g^{-1}, respectively.

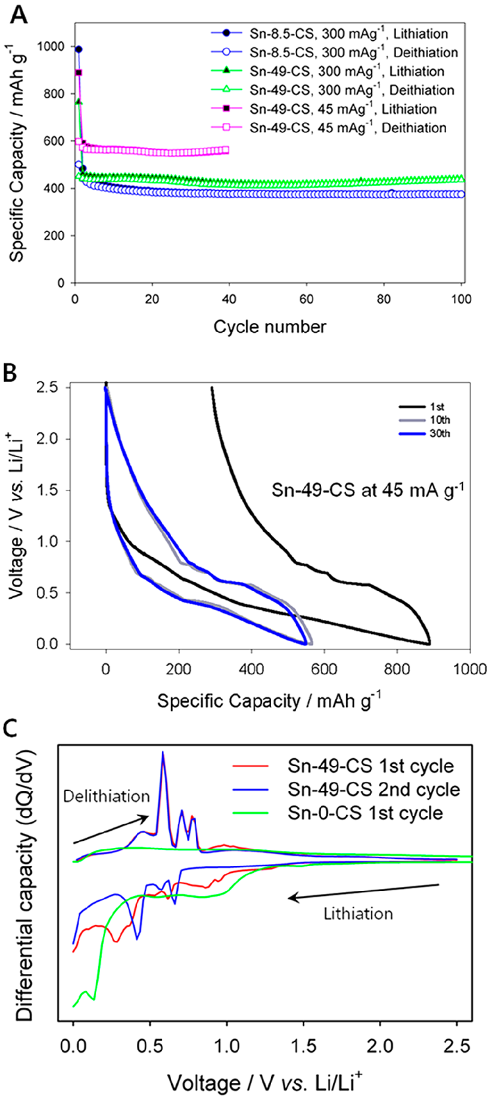

Figure 5. (A) Cycle performance of Sn-8.5-CS and Sn-49-CS electrodes. (B) Voltage profiles of Sn-49-CS electrodes at a current density of 45 mA g^{-1} (0.0–2.5 V *vs* Li/Li^+). The numbers 1st, 10th, and 30th indicate different cycles. (C) Differential capacity plot of delithiation voltage profiles (1st and 2nd cycle) for Sn-49-CS and Sn-0-CS electrodes at a current density of 45 mA g^{-1}.

The discharge (lithiation) and charge (delithiation) voltage profiles of a Sn-49-CS electrode are shown in Figure 5B and Figure S8. Three voltage plateaus occurring near 0.6 V are apparent in both profiles, reflecting that Li^+ insertion/deinsertion proceeds through three consecutive two-phase reactions. These voltage plateaus are typical characteristics of Sn electrodes.[47] These plateaus are represented as three peaks in the differential capacity plot (dQ/dV) of the Sn-49-CS electrode, as clearly shown in Figure 5C. Figure 5C also compared the differential capacities of Sn-49-CS with that of Sn-0-CS electrodes, and this indicates that the reversible capacity of Sn-49-CS is mainly contributed from the Sn nanoparticles, although the CS matrix (Sn-0-CS) is also an electrochemically active material, delivering *ca.* 400 mA h g^{-1} at 45 mA g^{-1} (Figure S9).

The theoretical capacity of Sn-49-CS is 690 mA h g^{-1}, assuming that both carbon matrix and Sn are fully utilized as an electrochemically active material, as shown in Table S1. The Sn-49-CS electrode delivers a reversible capacity of 600 mA h g^{-1} at 45 mA g^{-1}, and this indicates that 204 and 396 mA h g^{-1} are contributed from carbon and Sn, respectively, assuming that the carbon matrix is fully utilized. Thus, this means that, at least, 81% of Sn (808 mA h g_{Sn}^{-1} = 396/0.49) in the composite was utilized. In contrast to Sn-49-CS, plateaus in the voltage profiles of Sn-8.5-CS (Figure S10) are difficult to observe, which is attributable to the small amount of Sn content (8.5 wt %) in the composite.

Not only the three sharp peaks indicating Sn in the voltage range of 0.5−0.8 V are observed, but also a small hump is observable near 1 V during delithiation (Figure 5C). The small hump is related to the reversible SnO_x formation from Li_2O and Sn during delithiation.[7,8] In contrast to Sn-49-CS, the size of this hump is significantly large and distinguishably sharp in previous nanostructured SnO_2 anodes.[16] In our work, the integrated area (corresponding to a capacity) of the small hump is much smaller than that of the three sharp peaks in the dQ/dV plot. This indicates that the amount of SnO_x is much smaller than that of Sn in the composite, and the capacity obtained from SnO_x is negligible, even though the surface of Sn is partially oxidized, as shown in the XPS result (Figure S4).

The rate capabilities of the Sn-49-CS and Sn-8.5-CS electrodes are examined in Figure S11. Both electrodes show a good rate performance, but the rate capability of Sn-49-CS is slightly better than that of Sn-8.5-CS. Even at 3000 mA g^{-1}, the Sn-49-CS electrode exhibits 46% capacity retention of the capacity at 120 mA g^{-1}. The better rate performance of the Sn-49-CS electrode is attributed to its higher effective diffusion coefficient compared to the Sn-8.5-CS. The charge transfer resistance and effective diffusion coefficient values were obtained from the impedance fitting, as shown in Figure S12. The charge transfer resistance values of the Sn-49-CS and Sn-8.5-CS were 7.53×10^{-2} and 5.35×10^{-2} Ωg, respectively, and the effective diffusion coefficient values of the Sn-49-CS and Sn-8.5-CS were 4.18×10^{-13} and 8.58×10^{-14} $cm^2\ s^{-1}$, respectively. The lower charge transfer resistance of the Sn-8.5-CS than Sn-49-CS is attributed to the higher surface area of Sn-8.5-CS due to the lower loading amount of Sn in the composite. However, in spite of the lower charge transfer resistance of the Sn-8.5-CS than Sn-49-CS, the rate capability of the Sn-49-CS was better than the Sn-8.5-CS due to the higher effective diffusion coefficient of the Sn-49-CS. This indicates that the effective diffusion coefficient is a dominant factor in determining the rate performance of Sn-*x*-CS electrodes, as the rate-limiting step of lithium-ion batteries is known to be solid-state diffusion of lithium ions.

The Coulombic efficiency of all electrodes is over 99% except for the first few cycles. The Coulombic efficiency during the first cycle is 67.3, 50.7, and 42.8% for the Sn-49-CS, Sn-8.5-CS, and Sn-0-CS electrodes, respectively. The irreversible capacity decreases as the mass ratio of Sn/CS in the composites increases. This indicates that the large irreversible capacity is dominantly caused by electrolyte decomposition, forming a solid electrolyte interphase film on a carbon matrix with a large surface area. This is supported by the comparison of differential capacity plots (dQ/dV) of the Sn-49-CS electrode at the first and second cycle. During lithiation at the first cycle, the broad peak near 0.8 V is observed, but this peak disappears at the second cycle since the broad lithiation peak near 0.8 V at the first cycle is caused by the irreversible formation of SEI film.

CONCLUSIONS

In conclusion, we reported the tailored synthesis of Sn−CS composites with unique morphologies using a straightforward method with selective interaction among the precursors and PEO-*b*-PS. Metallic Sn species are homogeneously embedded in a rigid CS framework and are effectively confined with the morphologies of nanowires or nanoparticles depending on the initial TBPT loading. The resulting Sn−CS composite materials are successfully employed as anodes for LIBs and show superior reversible capacity and long cyclability. Most of all, the novel method developed in this work for synthesizing functional hybrid materials can be extended to the preparation of various functional nanocomposites owing to its versatility and facileness.

METHODS

Synthesis of Sn-*x*-CS Nanocomposites. PEO-*b*-PS[30] and resol[32] dissolved in THF (50 wt %) were synthesized according to the reported literature. The weight fraction of carbon and silica was fixed as 8:2, and the amount of Sn precursor was tuned to 8.5−49 wt % of Sn-embedded composite materials. For instance, to get 49 wt % of Sn−carbon−silica composite (Sn-49-CS), 0.15 g of PEO-*b*-PS (M_n = 37 040 g/mol, PDI = 1.07, 13.5 wt % of PEO) was first dissolved in 7 g of THF with 0.065 g of 0.2 M HCl. After 1 h of stirring, 0.136 g of TEOS, 0.628 g of 50 wt % resol in THF, and 0.969 g of tributylphenyltin (TBPT) were added in sequence. The mixture was further stirred for 1 h and poured into a Petri dish. THF was slowly evaporated at 30 °C for overnight or more to induce EISA (evaporation-induced self-assembly). Next, the dish was placed into an oven at 100 °C for 24 h or more to thermopolymerize the hybrid material. The thermopolymerization step further induced cross-linkage and polymerization of the resol resins and froze the overall frameworks. The as-made brownish-film-like products were scraped from the dish, and they were calcined in a tubular furnace at 450 °C for 2 h (further polymerization and stabilization) and subsequently heated at 700 °C for 2 h under N_2 atmosphere with a heating rate of 1 °C/min. The resulting black Sn−CS materials were ground into fine powders and used as anode materials for lithium-ion batteries. The yield of metallic Sn is near 82%, and the loss might be caused by vaporization of Sn precursor (TBPT) during the annealing at 100 °C and subsequent heat treatment. A small amount of liquid Sn can also be vaporized during heat treatment at 700 °C.

Electrochemical Characterization. The composite electrode was prepared by spreading a slurry mixture of Sn−CS powder, poly(acrylic acid) (PAA, as a binder), and super P (as a carbon additive for conductivity enhancement) (8:0.5:1.5 weight ratio) on a piece of Cu foil. The galvanostatic charge/discharge cycling was made in the potential range of 0.0−2.5 V with a two-electrode 2016-type coin cell, where Li metal foil was used as the counter electrode. Then, 1.3 M $LiPF_6$ in a mixture of ethylene carbonate (EC) and diethyl carbonate (DEC) (3:7 v/v) was used as the electrolyte. Polypropylene film was used as the separator. Cells were assembled in an Ar-filled glovebox and cycled at 30 °C. For impedance measurements using SP-200 (BioLogic), two-electrode cells were used, and the explored frequency range was from 500 kHz to 1 mHz under ac stimulus with 5 mV of amplitude. The impedance data were fitted using the Z view program.

Material Characterization. Gel permeation chromatography (GPC; Waters) was conducted using THF as the eluent, and the molecular weight was calibrated on the basis of PS standards. X-ray diffraction (XRD) data were collected using a MAX-2500 diffractometer (RIKAGU, Cu Kα, 1.54 Å). The morphology was observed using a transmission electron microscope (TEM; JEM-1011) operated at 80 kV. For TEM, the samples were microtomed with 100 nm section thickness. Micromeritics TristarII system at −196 °C was used to measure nitrogen physisorption. The samples were degassed overnight at 150 °C before measurement. Small-angle X-ray scattering (SAXS) experiments were carried out on the 4C1 SAXS beamline at the Pohang Light Source (PLS) using X-rays (7.8 keV, 0.16 nm). The actual Sn content of each composite was determined by inductively coupled plasma spectroscopy (ICP). A Raman spectrometer (Horiba Jobin Yvon, LabRam HR) was used with a laser at 514.532 nm (Ar-ion laser) at a power of 0.5 mW. X-ray photoelectron spectroscopy (XPS) was obtained by Quantera SXM/ULVAC-PHI.

Conflict of Interest: The authors declare no competing financial interest.

Acknowledgment. This work was supported by the National Research Foundation of Korea (NRF) grant funded by the Korea government (MEST) (No. 2012R1A2A2A01002879) and by the KRICT OASIS Project from Korea Research Institute of Chemical Technology. This work was further supported by the Global Frontier R&D Program on Center for Multiscale Energy System, which was funded by the National Research Foundation under the Ministry of Education, Science and Technology, Korea, and by the National Research Foundation of Korea (NRF) grant funded by the Korea Government (MEST) (No. 2012-0008827).

Supporting Information Available: Further characterization of Sn-*x*-CS composites such as the composition, TEM, BET, TGA, and XPS, hydrophilic, and hydrophobic content of the initial solution for the synthesis of Sn−CS, schematic representation of the decrease of surface-to-volume ratio, characterization of F127−Sn−CS, characterization of SnSb−CS composites, voltage profiles, rate capability, and impedance study of Sn-*x*-CS are included. This material is available free of charge *via* the Internet at http://pubs.acs.org.

REFERENCES AND NOTES

1. Tarascon, J. M.; Armand, M. Issues and Challenges Facing Rechargeable Lithium Batteries. *Nature* **2001**, *414*, 359–367.
2. Wang, Z.; Luan, D.; Boey, F. Y. C.; Lou, X. W. Fast Formation of SnO_2 Nanoboxes with Enhanced Lithium Storage Capability. *J. Am. Chem. Soc.* **2011**, *133*, 4738–4741.
3. Idota, Y.; Kubota, T.; Matsufuji, A.; Maekawa, Y.; Miyasaka, T. Tin-Based Amorphous Oxide: A High-Capacity Lithium-Ion-Storage Material. *Science* **1997**, *276*, 1395–1397.
4. Winter, M.; Besenhard, J. O. Electrochemical Lithiation of Tin and Tin-Based Intermetallics and Composites. *Electrochim. Acta* **1999**, *45*, 31–50.
5. Wachtler, M.; Besenhard, J. O.; Winter, M. Tin and Tin-Based Intermetallics as New Anode Materials for Lithium-Ion Cells. *J. Power Sources* **2001**, *94*, 189–193.
6. Courtney, I. A.; McKinnon, W.; Dahn, J. On the Aggregation of Tin in SnO Composite Glasses Caused by the Reversible Reaction with Lithium. *J. Electrochem. Soc.* **1999**, *146*, 59–68.
7. Lou, X. W.; Chen, J. S.; Chen, P.; Archer, L. A. One-Pot Synthesis of Carbon-Coated SnO_2 Nanocolloids with Improved Reversible Lithium Storage Properties. *Chem. Mater.* **2009**, *21*, 2868–2874.
8. Lou, X. W.; Li, C. M.; Archer, L. A. Designed Synthesis of Coaxial SnO_2@Carbon Hollow Nanospheres for Highly Reversible Lithium Storage. *Adv. Mater.* **2009**, *21*, 2536–2539.
9. Egashira, M.; Takatsuji, H.; Okada, S.; Yamaki, J. Properties of Containing Sn Nanoparticles Activated Carbon Fiber for a Negative Electrode in Lithium Batteries. *J. Power Sources* **2002**, *107*, 56–60.
10. Lee, K. T.; Jung, Y. S.; Oh, S. M. Synthesis of Tin-Encapsulated Spherical Hollow Carbon for Anode Material in Lithium Secondary Batteries. *J. Am. Chem. Soc.* **2003**, *125*, 5652–5653.
11. Jung, Y. S.; Lee, K. T.; Ryu, J. H.; Im, D.; Oh, S. M. Sn-Carbon Core−Shell Powder for Anode in Lithium Secondary Batteries. *J. Electrochem. Soc.* **2005**, *152*, A1452–A1457.
12. Derrien, G.; Hassoun, J.; Panero, S.; Scrosati, B. Nanostructured Sn−C Composite as an Advanced Anode Material in High-Performance Lithium-Ion Batteries. *Adv. Mater.* **2007**, *19*, 2336–2340.
13. Deng, D.; Lee, J. Y. Reversible Storage of Lithium in a Rambutan-like Tin−Carbon Electrode. *Angew. Chem., Int. Ed.* **2009**, *48*, 1660–1663.
14. Yu, Y.; Gu, L.; Zhu, C.; van Aken, P. A.; Maier, J. Tin Nanoparticles Encapsulated in Porous Multichannel Carbon Microtubes: Preparation by Single-Nozzle Electrospinning and Application as Anode Material for High-Performance Li-Based Batteries. *J. Am. Chem. Soc.* **2009**, *131*, 15984–15985.
15. Yu, Y.; Gu, L.; Wang, C.; Dhanabalan, A.; van Aken, P. A.; Maier, J. Encapsulation of Sn@ Carbon Nanoparticles in Bamboo-like Hollow Carbon Nanofibers as an Anode Material in Lithium Based Batteries. *Angew. Chem., Int. Ed.* **2009**, *48*, 6485–6489.
16. Han, S.; Jang, B.; Kim, T.; Oh, S. M.; Hyeon, T. Simple Synthesis of Hollow Tin Dioxide Microspheres and Their Application to Lithium-Ion Battery Anodes. *Adv. Funct. Mater.* **2005**, *15*, 1845–1850.
17. Zou, Y.; Wang, Y. Sn@ CNT Nanostructures Rooted in Graphene with High and Fast Li-Storage Capacities. *ACS Nano* **2011**, *5*, 8108–8114.
18. Hassoun, J.; Derrien, G.; Panero, S.; Scrosati, B. A Nanostructured Sn−C Composite Lithium Battery Electrode with Unique Stability and High Electrochemical Performance. *Adv. Mater.* **2008**, *20*, 3169–3175.
19. Luo, B.; Wang, B.; Liang, M.; Ning, J.; Li, X.; Zhi, L. Reduced Graphene Oxide-Mediated Growth of Uniform Tin-Core/Carbon-Sheath Coaxial Nanocables with Enhanced Lithium Ion Storage Properties. *Adv. Mater.* **2012**, *24*, 1405–1409.
20. Lee, J.; Yoon, S.; Hyeon, T.; Oh, S. M.; Kim, K. B. Synthesis of a New Mesoporous Carbon and Its Application to Electrochemical Double-Layer Capacitors. *Chem. Commun.* **1999**, 2177–2178.
21. Lee, J.; Kim, J.; Hyeon, T. Recent Progress in the Synthesis of Porous Carbon Materials. *Adv. Mater.* **2006**, *18*, 2073–2094.
22. Wan, Y.; Yang, H.; Zhao, D. `Host−Guest' Chemistry in the Synthesis of Ordered Nonsiliceous Mesoporous Materials. *Acc. Chem. Res.* **2006**, *39*, 423–432.
23. Zhu, S.; Zhou, H.; Hibino, M.; Honma, I.; Ichihara, M. Synthesis of MnO_2 Nanoparticles Confined in Ordered

Mesoporous Carbon Using a Sonochemical Method. *Adv. Funct. Mater.* **2005**, *15*, 381–386.

24. Ji, X.; Lee, K. T.; Nazar, L. F. A Highly Ordered Nanostructured Carbon–Sulphur Cathode for Lithium–Sulphur Batteries. *Nat. Mater.* **2009**, *8*, 500–506.
25. Kang, E.; Jung, Y. S.; Cavanagh, A. S.; Kim, G. H.; George, S. M.; Dillon, A. C.; Kim, J. K.; Lee, J. Fe_3O_4 Nanoparticles Confined in Mesocellular Carbon Foam for High Performance Anode Materials for Lithium Ion Batteries. *Adv. Funct. Mater.* **2011**, *21*, 2430–2438.
26. Kim, H.; Cho, J. Superior Lithium Electroactive Mesoporous Si@Carbon Core–Shell Nanowires for Lithium Battery Anode Material. *Nano Lett.* **2008**, *8*, 3688–3691.
27. Kang, E.; Jung, H.; Park, J. G.; Kwon, S.; Shim, J.; Sai, H.; Wiesner, U.; Kim, J. K.; Lee, J. Block Copolymer Directed One-Pot Simple Synthesis of L10-Phase FePt Nanoparticles inside Ordered Mesoporous Aluminosilicate/Carbon Composites. *ACS Nano* **2011**, *5*, 1018–1025.
28. Shim, J.; Lee, J.; Ye, Y.; Hwang, J.; Kim, S. K.; Lim, T. H.; Wiesner, U.; Lee, J. One-Pot Synthesis of Intermetallic Electrocatalysts in Ordered, Large-Pore Mesoporous Carbon/Silica toward Formic Acid Oxidation. *ACS Nano* **2012**, *6*, 6870–6881.
29. Matyjaszewski, K.; Xia, J. H. Atom Transfer Radical Polymerization. *Chem. Rev.* **2001**, *101*, 2921–2990.
30. Hwang, J.; Kim, J.; Ramasamy, E.; Choi, W.; Lee, J. Easy Access to Highly Crystalline Mesoporous Transition-Metal Oxides with Controllable Uniform Large Pores by Using Block Copolymers Synthesized *via* Atom Transfer Radical Polymerization. *Microporous Mesoporous Mater.* **2011**, *143*, 149–156.
31. Lee, J.; Orilall, M.; Warren, S.; Kamperman, M.; DiSalvo, F.; Wiesner, U. Direct Access to Thermally Stable and Highly Crystalline Mesoporous Transition-Metal Oxides with Uniform Pores. *Nat. Mater.* **2008**, *7*, 222–228.
32. Liu, R.; Shi, Y.; Wan, Y.; Meng, Y.; Zhang, F.; Gu, D.; Chen, Z.; Tu, B.; Zhao, D. Triconstituent Co-assembly to Ordered Mesostructured Polymer–Silica and Carbon–Silica Nanocomposites and Large-Pore Mesoporous Carbons with High Surface Areas. *J. Am. Chem. Soc.* **2006**, *128*, 11652–11662.
33. Templin, M.; Franck, A.; Du Chesne, A.; Leist, H.; Zhang, Y.; Ulrich, R.; Schadler, V.; Wiesner, U. Organically Modified Auminosilicate Mesostructures from Block Copolymer Phases. *Science* **1997**, *278*, 1795–1798.
34. Simon, P. F. W.; Ulrich, R.; Spiess, H. W.; Wiesner, U. Block Copolymer-Ceramic Hybrid Materials from Organically Modified Ceramic Precursors. *Chem. Mater.* **2001**, *13*, 3464–3486.
35. Huang, Y.; Liu, H.; Hu, Y. Morphologies of Diblock Copolymer/Homopolymer Blend Films. *Macromol. Theory Simul.* **2006**, *15*, 321–330.
36. Hashimoto, T.; Kimishima, K.; Hasegawa, H. Self-Assembly and Patterns in Binary Mixtures of SI Block Copolymer and PPO. *Macromolecules* **1991**, *24*, 5704–5712.
37. Matsen, M. Phase Behavior of Block Copolymer/Homopolymer Blends. *Macromolecules* **1995**, *28*, 5765–5773.
38. Semenov, A. Phase Equilibria in Block Copolymer-Homopolymer Mixtures. *Macromolecules* **1993**, *26*, 2273–2281.
39. Schmidt-Winkel, P.; Lukens, W. W., Jr.; Zhao, D.; Yang, P.; Chmelka, B. F.; Stucky, G. D. Mesocellular Siliceous Foams with Uniformly Sized Cells and Windows. *J. Am. Chem. Soc.* **1999**, *121*, 254–255.
40. Lettow, J. S.; Han, Y. J.; Schmidt-Winkel, P.; Yang, P.; Zhao, D.; Stucky, G. D.; Ying, J. Y. Hexagonal to Mesocellular Foam Phase Transition in Polymer-Templated Mesoporous Silicas. *Langmuir* **2000**, *16*, 8291–8295.
41. Wang, Y.; Lee, J. Y.; Deivaraj, T. C. Tin Nanoparticle Loaded Graphite Anodes for Li-Ion Battery Applications. *J. Electrochem. Soc.* **2004**, *151*, A1804–A1809.
42. Nayral, C.; Viala, E.; Fau, P.; Senocq, F.; Jumas, J. C.; Maisonnat, A.; Chaudret, B. Synthesis of Tin and Tin Oxide Nanoparticles of Low Size Dispersity for Application in Gas Sensing. *Chem.—Eur. J.* **2000**, *6*, 4082–4090.
43. Zheng, T.; Zhong, Q.; Dahn, J. High-Capacity Carbons Prepared from Phenolic Resin for Anodes of Lithium-Ion Batteries. *J. Electrochem. Soc.* **1995**, *142*, L211–L214.
44. Dahn, J.; Zheng, T.; Yinghu, L.; Xue, J. Mechanisms for Lithium Insertion in Carbonaceous Materials. *Science* **1995**, *270*, 590–593.
45. Schwan, J.; Ulrich, S.; Batori, V.; Ehrhardt, H.; Silva, S. Raman Spectroscopy on Amorphous Carbon Films. *J. Appl. Phys.* **1996**, *80*, 440–447.
46. Ferrari, A.; Robertson, J. Interpretation of Raman Spectra of Disordered and Amorphous Carbon. *Phy. Rev. B* **2000**, *61*, 14095–14107.
47. Courtney, I.; Tse, J.; Mao, O.; Hafner, J.; Dahn, J. *Ab Initio* Calculation of the Lithium-Tin Voltage Profile. *Phys. Rev. B* **1998**, *58*, 15583–15588.